Current Research in Structural Biology 3 (2021) 72–84

Contents lists available at ScienceDirect

Current Research in Structural Biology

journal homepage: www.journals.elsevier.com/current-research-in-structural-biology

Biochemical and structural characterization of two cif-like epoxide hydrolases from *Burkholderia cenocepacia*

Noor M. Taher [a], Kelli L. Hvorecny [a,1], Cassandra M. Burke [a], Morgan S.A. Gilman [a,2], Gary E. Heussler [b,3], Jared Adolf-Bryfogle [c,d,e], Christopher D. Bahl [c,d,e], George A. O'Toole [b], Dean R. Madden [a,*]

[a] Department of Biochemistry and Cell Biology, Geisel School of Medicine at Dartmouth, Hanover, NH, USA
[b] Department of Microbiology and Immunology, Geisel School of Medicine at Dartmouth, Hanover, NH, USA
[c] Institute for Protein Innovation, Boston, MA, USA
[d] Division of Hematology/Oncology, Boston Children's Hospital, Boston, MA, USA
[e] Department of Pediatrics, Harvard Medical School, Boston, MA, USA

ARTICLE INFO

Keywords:
α/β hydrolase
X-ray crystallography
Burkholderia cenocepacia
Epoxy-polyunsaturated fatty acids
Epoxide hydrolase

ABSTRACT

Epoxide hydrolases catalyze the conversion of epoxides to vicinal diols in a range of cellular processes such as signaling, detoxification, and virulence. These enzymes typically utilize a pair of tyrosine residues to orient the substrate epoxide ring in the active site and stabilize the hydrolysis intermediate. A new subclass of epoxide hydrolases that utilize a histidine in place of one of the tyrosines was established with the discovery of the CFTR Inhibitory Factor (Cif) from *Pseudomonas aeruginosa*. Although the presence of such Cif-like epoxide hydrolases was predicted in other opportunistic pathogens based on sequence analyses, only Cif and its homolog aCif from *Acinetobacter nosocomialis* have been characterized. Here we report the biochemical and structural characteristics of Cfl1 and Cfl2, two Cif-like epoxide hydrolases from *Burkholderia cenocepacia*. Cfl1 is able to hydrolyze xenobiotic as well as biological epoxides that might be encountered in the environment or during infection. In contrast, Cfl2 shows very low activity against a diverse set of epoxides. The crystal structures of the two proteins reveal quaternary structures that build on the well-known dimeric assembly of the α/β hydrolase domain, but broaden our understanding of the structural diversity encoded in novel oligomer interfaces. Analysis of the interfaces reveals both similarities and key differences in sequence conservation between the two assemblies, and between the canonical dimer and the novel oligomer interfaces of each assembly. Finally, we discuss the effects of these higher-order assemblies on the intra-monomer flexibility of Cfl1 and Cfl2 and their possible roles in regulating enzymatic activity.

1. Introduction

Epoxide hydrolases (EHs) catalyze the conversion of a variety of epoxides to their corresponding vicinal diols by the addition of a water molecule. These enzymes serve a variety of functions that generally fall under two themes; neutralizing detrimental epoxides, and processing epoxides as part of normal cellular physiology. For example, FosX, an enzyme that hydrolyzes fosfomycin, confers resistance to this natural antibiotic (Fillgrove et al., 2003; Scortti et al., 2018). *Mycobacterium tuberculosis*'s EphD is involved in the metabolism of mycolic acid, which is a key element of mycobacteria's cell wall (Madacki et al., 2018). Two of the most extensively studied EHs are the human soluble EH (sEH) and microsomal EH (mEH). sEH is mainly involved in processing fatty-acid epoxides that mediate numerous signals, including the regulation of pain, inflammation, and blood pressure (Decker et al., 2009). mEH detoxifies reactive epoxides, e.g., from the environment or from metabolic activity (Vaclavikova et al., 2015). Both sEH and mEH are therapeutic targets in multiple diseases (Barnych et al., 2020; Wagner et al., 2017).

* Corresponding author. 7200 Vail Building, Room 408, Hanover, NH, 03755-3844, USA.
E-mail address: dean.r.madden@dartmouth.edu (D.R. Madden).
[1] Present address: Kelli L. Hvorecny, Department of Biochemistry, University of Washington, Seattle, WA, USA.
[2] Present address: Morgan S.A. Gilman, Department of Biological Chemistry and Molecular Pharmacology, Blavatnik Institute, Harvard Medical School, Boston, MA, USA.
[3] Present address: Gary E. Heussler, Division of Biological Sciences, University of California, San Diego, La Jolla, United States.

https://doi.org/10.1016/j.crstbi.2021.02.002
Received 9 September 2020; Received in revised form 25 January 2021; Accepted 12 February 2021

EHs that belong to the α/β hydrolase superfamily of enzymes utilize an Asp-His-Asp/Glu catalytic triad to open the epoxide ring substrate and release the vicinal diol product. In addition to the catalytic triad, the active site of these enzymes usually contains two conserved tyrosine residues (the "Tyr-Tyr pair") that orient the substrate epoxide ring in the active site pocket and form an oxyanion hole to stabilize a hydrolysis intermediate (Yamada et al., 2000). However, a new subclass of epoxide hydrolases that utilize a His-Tyr pair instead of the canonical Tyr-Tyr pair was revealed with the discovery of the CFTR Inhibitory Factor (Cif) from *Pseudomonas aeruginosa* (Bahl and Madden, 2012).

Cif is an epoxide hydrolase from *P. aeruginosa* that serves as a virulence factor in lung infections. Cif has been shown to decrease the concentration of the Cystic Fibrosis Transmembrane Conductance Regulator (CFTR) on the apical surface of lung epithelial cells, sabotage the inflammation resolution signaling between the epithelial cells and the immune system, and hinder mucociliary clearance of bacteria (Flitter et al., 2017; Hvorecny et al., 2018; MacEachran et al., 2007). The crystal structure of Cif showed that it utilizes a His-Tyr pair instead of the canonical Tyr-Tyr pair for epoxide ring orientation and hydrolysis intermediate stabilization (Bahl et al., 2010). aCif from *Acinetobacter nosocomialis* was subsequently shown to belong to this new class of Cif-like (Cfl) epoxide hydrolases (Bahl et al., 2014). While Cif and aCif have been characterized structurally and biochemically, Cfls present in other opportunistic pathogens remain uncharacterized.

Burkholderia cenocepacia is a gram-negative bacterium that belongs to the *Burkholderia cepacia* complex. *B. cenocepacia* encounters diverse environments where its presence has important implications. It is commonly found in the soil where it can cause plant infections, serve as a biocontrol agent to prevent plant infections, and degrade aromatic hydrocarbon compounds (Juhasz et al., 1997; Huang and Wong, 1998; Jacobs et al., 2008; Krumme et al., 1993; Chen et al., 2020; Khodai-Kalaki et al., 2015). *B. cenocepacia* can also colonize the lung extracellular milieu of immunocompromised and non-immunocompromised patients, where it causes high morbidity and mortality, in part due to its broad antibiotic resistance (Agodi et al., 2002; Belchis et al., 2000; Scoffone et al., 2017). The bacteria are also able to cause a systemic infection by entering the patient's bloodstream, a condition known "Cepacia Syndrome" (Kalferstova et al., 2015). *B. cenocepacia* therefore seems well adapted for survival in a wide range of environments where it must process and respond to a variety of signals and metabolites, including epoxides. However, no epoxide hydrolases from *B. cenocepacia* have been characterized to date. Additionally, whereas it is known that *P. aeruginosa* can use Cif to hydrolyze 14,15-epoxy-eicosatrienoic acid (14,15-EET) to intercept downstream pro-resolution effects and exacerbate the host's inflammatory response (Flitter et al., 2017), it is not known whether *B. cenocepacia* possesses Cfls with such anti-resolution potential.

Here we characterize two predicted Cfls from *B. cenocepacia,* named Cfl1 and Cfl2. We demonstrate that Cfl1 possesses epoxide hydrolysis activity against xenobiotic and potential host-derived epoxides. While Cif and aCif exist as constitutive dimers, our hydrodynamic and structural studies revealed that Cfl1 and Cfl2 exist as octamers and decamers, respectively, by forming rings of dimers. Although the overall assembly of each higher-order Cfl oligomer is similar, detailed structural analysis revealed key differences between the oligomer as well as the dimer interfaces of each assembly. We finally discuss the possible role of the differential steric constraints placed on the monomer subunit in each structure in regulating enzyme activity.

2. Results

2.1. Bcen_3967 and Bcen_4419 are Cif-like predicted epoxide hydrolases

In *B. cenocepacia* strain HI2424, the two proteins with the highest amino-acid sequence identity to Cif are encoded by *Bcen_3967* (34% identical, hereafter named Cfl1) and *Bcen_4419* (32% identical, hereafter named Cfl2). Amino-acid sequence alignment with Cif shows that both proteins are predicted to have the catalytic residues required for epoxide hydrolysis (Fig. 1). Cfl1 and Cfl2 also appear to utilize a Cif-like His-Tyr epoxide ring-opening pair instead of the classical Tyr-Tyr pair. In addition to the catalytic residues, canonical epoxide hydrolases are also distinguished by an H-G-X-P motif, where X tends to be an aromatic residue and P is a *cis*-proline (van Loo et al., 2006). The H-G-W-P sequence of Cfl1 follows the canonical H-G-X-P motif, whereas Cfl2 substitutes the histidine with an alanine (A-G-F-P). Finally, whereas Cif has an N-terminal secretion signal to direct its export from the cell, neither Cfl1 nor Cfl2 is predicted to have such signal (Fig. 1).

2.2. B. cenocepacia HI2424 upregulates the transcription of Cfl2, but not Cfl1, in response to certain epoxides

In *P. aeruginosa* strain PA14, *cif* is part of a three-gene operon that is under regulation by CifR, a TetR-like transcriptional repressor. CifR binds to the intergenic region between *cifR* and the *cif* operon and represses transcription of the operon. The presence of certain epoxides in the medium causes CifR to release the DNA and de-repress *cif* transcription (Ballok et al., 2012; MacEachran et al., 2008). *A. nosocomialis* uses a similar epoxide-sensitive regulatory circuit to control the transcription of its *cif* gene (Bahl et al., 2014). Similarly, *cfl1* and *cfl2* each reside near a gene coding for a TetR-like protein (Fig. 2(A)). However, unlike the divergent transcription seen for *cifR* and *cif*, both the *cfl1/cfl1R* and *cfl2/cfl2R* genes appear to be transcribed in the same direction, and two other members of the *cif* operon in PA14 - *morB* and the MFS transporter gene - are absent from the putative operons of *cfl1/2* (Fig. 2(A)). Given the similarities and differences between the *cif* and *cfl1/2* operons, we sought to determine whether the transcription of *cfl1* and *cfl2* is similarly upregulated in response to epoxides. We found that exposure of *B. cenocepacia* HI2424 to epibromohydrin (EBH), *R*-styrene oxide (*R*–SO), and *S*–SO increases transcription of *cfl2* by approximately 5 fold, 15 fold, and 3 fold, respectively, relative to the dimethyl sulfoxide vehicle control (DMSO) as measured by RT-qPCR (Fig. 2(B)). In contrast, the same treatments do not result in significantly increased transcription of *cfl1* (Fig. 2(B)).

2.3. Biochemical characterization of Cfl1 and Cfl2

In order to characterize the enzymatic activities and structures of Cfl1 and Cfl2, we sought to express and purify the two proteins heterologously. Both proteins were overexpressed in *E. coli* BL21(DE3) cells C-terminal to a 10 × His-SUMO tag, but only Cfl2 was found in the soluble fraction of the cell lysate. After unsuccessful troubleshooting attempts to obtain soluble Cfl1, we shifted our strategy towards finding a Cfl1 homolog in other *B. cenocepacia* strains with high sequence identity and soluble expression. We found the desired properties in CAR55383.1 from *B. cenocepacia* strain J2315, which exhibits 92% amino-acid sequence identity to Cfl1 (Fig. S1). Hereafter "Cfl1" refers to Cfl1 from strain J2315, unless otherwise noted.

Following scarless tag cleavage by the SUMO protease Ulp1 (Lau et al., 2018), Cfl1 and Cfl2 both eluted from a size-exclusion chromatography (SEC) column as large species, with Cfl1 eluting later than Cfl2 (Fig. 3(A)). Calibration of the Superdex 200 10/300 SEC column with standards of known relative molar mass (M_r) revealed that Cfl1 and Cfl2 peak elution volumes fall between those of apoferritin (440 kDa) and β-amylase (200 kDa), with predicted M_r values of 240 kDa and 350 kDa, respectively. These elution volumes are constant over concentrations ranging from ~2 μM to 200 μM, with no indication of smaller species (e.g., dimers; data not shown). Since the apparent M_r estimates obtained from SEC can be influenced by the shape of the particles in addition to their actual mass, we combined the diffusion coefficients obtained from SEC with the sedimentation coefficients obtained by velocity sedimentation analytical ultracentrifugation in order to gain a more shape-independent estimate of relative molar masses for Cfl1 and Cfl2 (Fig. 3(B) and Eq. 1, Materials and Methods). With a sedimentation

```
Cif          MILDRLCRGLLAGIALTFSLGGFAAEEFPVPNGFESAYREVDGVKLHYVKGGQ--GPLVM 58
Cfl1         ------MQNEPSMSGMPAPGLPAGFDR-----RFSRRYAQVDDVRLHYVTGGPDDGELVV 49
Cfl2         ------MYQHQSTEAASHLEATPYFREDPRLTGFRHRFDTVDGVRLHFVEGGRADGETIV 54
                           :                          *   :  ** *:**:* **   *  ::

Cif          LVHGFGQTWYEWHQLMPELAKR-FTVIAPDLPGLGQSEPPKTGYSGEQVAVYLHKLARQF 117
Cfl1         LLHGWPQTWYTWRHVMPVLAQEGYRVVAVDYRGAGESDKPLGGYDKASMAGDIRALVRQL 109
Cfl2         LLAGFPESWYAWRRVMPLLADE-FRIVAPDLPGQGDSDRPLVGYDTQTVAATLARLLERQ 113
             *: *: ::** *:::** **   : ::* *  * *:*: *  **    :*  :  *  :

Cif          SPDRPFDLVAHDIGIWNTYPMVVKNQADIARLVYMEAPIPDARIYRFPAFTAQGESLVWH 177
Cfl1         GATR-IHLVGRDIGVMVAYAYAAQRPAEIVKLAMLDVPVPGTRIWDEAKARADP--QIWH 166
Cfl2         NIAR-FYLAAHDVGAWVAYPFAAMYPESVKRLALLDAGIPGVTLPAALPIEPGNAWRTWH 172
                * : *  :*:*   :*          : :*  ::  :*   :              **

Cif          FSFFAADDRLAETLIAGKERFFLEHFIKSHSSNTEVFSERLLDLYARSYAKPHSLNASFE 237
Cfl1         FGLHQQRD-IAELLIAGKEHAYILDFYKKRAH--VALSNDDIAVYADAYAAPGALRAGFE 223
Cfl2         FAFHTVAD-LPETLIAGKEREYLDWFLRRKAANPESFSDADVDEYLRVFTRDGGLRAGLA 231
             * :    * : * ******: ::  * : ::     :*:  :  *   ::    * * :

Cif          YYRALNESVRQNAELAKT-RLQMPTMTLAGGGHGGMGTFQLEQMKAYADDVEGHVLPGCG 296
Cfl1         LYRAFPQDETQFKAFMKH-KLPMPVLALAG--DKSNGAKEFDMAKELALDVRGAVAPNTG 280
Cfl2         FYRAVSESSAQNRKLQALGKLKMPVLAVSA--DQGSIPDMAGPLEHVAEEVTAATIAYSG 289
              ***  :   *   :    :* ** ::::              :  * :*        *

Cif          HWLPEECAAPMNRLVIDFLSRGR--- 319
Cfl1         HWLPDENPAFLTRQLLDFFREPAPNR 306
Cfl2         HFIPEEQPQALARELRDFFR------ 309
             *::*:*    : * : **:
```

Fig. 1. Cfl1 and Cfl2 amino-acid sequences contain Cif-like epoxide hydrolase sequence motifs. ClustalW was used to align the amino-acid sequences of Cif from *P. aeruginosa* strain PA14 with Cfl1 and Cfl2 from *B. cenocepacia* strain HI2424. The residues corresponding to the canonical epoxide hydrolase H-G-X-P motif and the core catalytic residues are highlighted in bold blue and bold red, respectively. The secretion signal sequence of Cif is highlighted in bold magenta. Asterisks and colons below each position indicate identity and similarity among the three sequences, respectively. (For interpretation of the references to colour in this figure legend, the reader is referred to the web version of this article.)

coefficient of 10.2 S for Cfl1 and 11.2 S for Cfl2, Equation 1 yields M_r estimates of 260 kDa and 320 kDa, respectively. Since the predicted M_r for a monomer of both proteins is ~34.5 kDa, these results indicate that Cfl1 and Cfl2 exist as higher order oligomers compared to the dimeric Cif and aCif. Finally, we used circular dichroism spectroscopy to examine the thermal stability of the two proteins and determined that Cfl1 and Cfl2 oligomers are both stable well beyond physiologically relevant temperatures (Fig. 3(C) and (D)). Cfl2 shows a melting temperature of ~70 °C, and is substantially unfolded at 85 °C; Cfl1 shows no major sigmoidal change in molar ellipticity at 222 nm up to 90 °C and retains most dichroic characteristics of its folded structure at 85 °C.

2.4. Epoxide hydrolysis activity of Cfl1 and Cfl2

Given the presence of the epoxide-hydrolase signature motif in the amino-acid sequences of Cfl1 and Cfl2, we performed a preliminary screen for their catalytic activity against a selection of xenobiotic and biologically relevant epoxides using the adrenochrome reporter endpoint assay (Cedrone et al., 2005). Cfl1 hydrolyzed the *R* enantiomer of SO, and its activity against *S*–SO was significant but nonetheless reduced compared to the *R*–SO reaction (Fig. 4). Cfl1 showed very low levels of activity against other epoxides (Supplementary Table 1). Surprisingly, Cfl2 had very low activity against all of the tested substrates despite using relatively high protein concentrations (20–80 μM) and long incubation periods (1–2 h) in the endpoint assay (Fig. 4, Table S1). While quantitative comparisons are difficult in an endpoint assay, the level of Cfl2 activity against the tested substrates is comparable to the level of activity aCif showed against epoxides that were deemed non-substrates for that epoxide hydrolase (Bahl et al., 2014), although slightly higher levels were observed for Cfl2 with glycidol and *cis*-stilbene oxide. Cfl1 amino-acid sequence alignment with Cif suggests that Asp123 is responsible for the nucleophilic attack that opens the epoxide ring. To test this hypothesis, we expressed and purified a mutant Cfl1 in which Asp123 was substituted with a serine (Cfl1-D123S). Although hydrolysis of *R*–SO by the mutant formally crosses the threshold of statistical significance, the low absolute level of hydrolysis measured is unlikely to be catalytically meaningful and is sharply decreased compared to the wild-type hydrolysis of *R*–SO, consistent with our mechanistic hypothesis (Fig. 4).

Cif can convert polyunsaturated epoxide fatty acids upstream of pro-resolving signals into their vicinal diol counterparts (Hvorecny et al., 2017). *P. aeruginosa* strain PA14 can utilize that capability of Cif to intercept pro-resolving signal pathways between lung epithelial cells and immune cells, ultimately leading to a cycle of host tissue injury and further inflammation (Flitter et al., 2017). We were interested in determining whether Cfl1 possesses similar activity towards physiologically important host-derived substrates. We compared the hydrolytic activity of wild-type Cfl1 and Cfl1-D123S against a panel of four human-derived epoxides that are known signaling molecules *in vivo* (Jung et al., 2012; VanRollins, 1995; Ye et al., 2002; Zhang et al., 2001). The four epoxides vary in length, number of double bonds, and the position of the epoxide moiety along the hydrocarbon chain. Wild-type Cfl1 showed significantly more activity against these epoxides compared to Cfl1-D123S (Fig. 5).

2.5. Structural characterization of Cfl1 and Cfl2

To obtain a first look at the architecture of these proteins, we used electron microscopy of negatively stained single particles to examine the

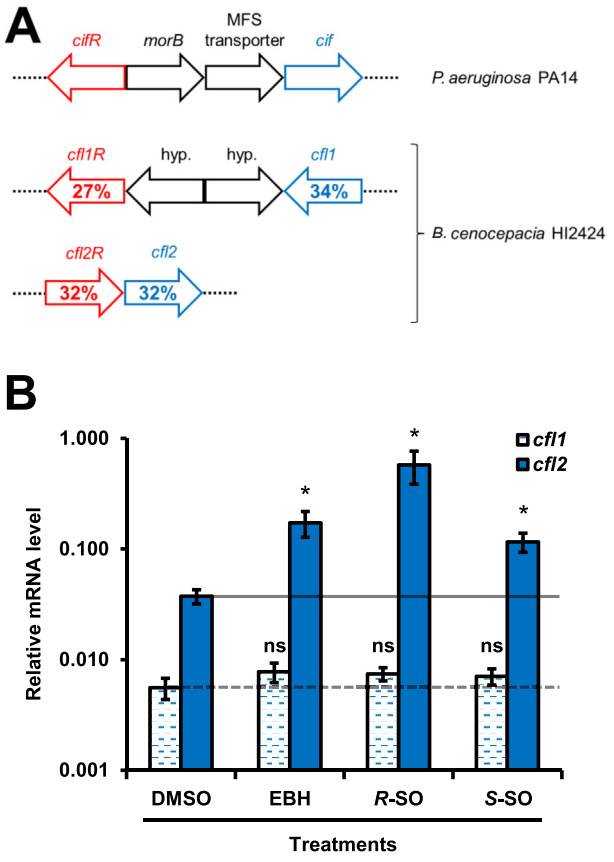

Fig. 2. *B. cenocepacia* strain HI2424 upregulates the transcription of *cfl2* in the presence of epoxides in the growth medium. (A) The *cif* operon in *P. aeruginosa* strain PA14 and the genomic regions in *B. cenocepacia* strain HI2424 that encompass *cfl1-cfl1R* and *cfl2-cfl2R* genes are shown. The percent amino-acid sequence identities of Cfl1 and Cfl2 to Cif (blue) and of Cfl1R and Cfl2R to CifR (red) calculated using EMBOSS Needle (Needleman and Wunsch, 1970) are indicated on the corresponding genes. (B) Relative mRNA levels of *cfl1* and *cfl2* in *B. cenocepacia* strain HI2424 treated with various epoxides (EBH, epibromohydrin; *R*–SO, *R*-styrene oxide; *S*–SO, *S*-styrene oxide) or control (DMSO, dimethylsulfoxide) were measured using RT-qPCR. The change in measured transcript levels of *cfl1* and *cfl2* between treatments was normalized to the levels of *rplU*. Values are reported on a $\log_{10}$ scale as the means of three experiments, and the error bars represent the standard deviation. Buffer and substrate-only controls are shown in grey. An asterisk indicates $p < 0.05$ when Student's unpaired *t*-test was used to compare mRNA levels between epoxide-treated and DMSO-treated bacteria (n = 3). ns, not signficant. (For interpretation of the references to colour in this figure legend, the reader is referred to the web version of this article.)

overall shape of Cfl2. As shown in Fig. S2 (top panel), a representative raw micrograph of Cfl2 particles shows that they adopt a ring-like structure with a central hole, seen when these molecules adhere to the grid in a "face-on" orientation. Class averages confirm this observation, with some class averages also showing a rectangular shape, which is presumably the "side-on" orientation (Fig. S2, bottom panels).

In order to obtain a more detailed picture of the structures of Cfl1 and Cfl2, we determined the crystal structures of both proteins to 2.2 Å resolution (Table 1). Each monomer of Cfl1 and Cfl2 exhibits the typical tertiary structure of the α/β hydrolase superfamily, with the main-chain atom RMSD between Cfl1 and Cif being 0.8 Å and between Cfl2 and Cif being 1.2 Å (Fig. 6(A) and (B)). When we compared the Cfl1 and Cif active sites, we observed two unique features in Cfl1 (Fig. 6(A), inset). First, Asp147, the Cfl1 residue presumed to be the charge-relay acid according to the pairwise sequence alignment with Cif, is not hydrogen bonded with His284, as is typical in acid-base-nucleophile catalytic triads. Instead, that hydrogen bond with His284 is satisfied by Ser258. The side chain of Asp147 is oriented in the opposite direction compared to Cif's Glu153 and forms a salt bridge with Arg122, which aligns to His128 in Cif. The second unique feature of the Cfl1 active site is that Arg122 forms a hydrogen bond with the catalytic water. In Cif, the equivalent residue His128 does not form a hydrogen bond with the catalytic water. In contrast to Cfl1, the catalytic side chains of Cfl2 show a much more similar alignment those of Cif (Fig. 6(B), inset).

Consistent with the negative-stain electron microscopy and hydrodynamic studies, Cfl1 and Cfl2 form higher-order oligomers, either octamers or decamers, respectively, arranged in a ring-like fashion (Fig. 7(A) and (C)). Each assembly is formed by a ring of dimers: a tetrameric ring of dimers in the case of Cfl1, and a pentameric ring in the case of Cfl2. The dimeric subunits of Cfl1 and Cfl2 that are equivalent to the Cif dimer are highlighted in Fig. 7(B) (grey) and Fig. 7(D) (yellow). Like the Cif dimer, the canonical Cfl1 and Cfl2 dimer is formed through cap domain interactions between two monomers. Unlike Cif, however, each monomer in Cfl1 and Cfl2 has additional oligomerization interfaces that drive the cyclization of the dimer subunits to form the ring-like structures.

For an initial, higher-level comparison between the Cfl1 and Cfl2 oligomers, we analyzed their interfaces using Rosetta (Table 2) (Fleishman et al., 2011; Khatib et al., 2011; Lawrence and Colman, 1993; Pavlovicz et al., 2020). The most striking difference is in the canonical dimer (1:2) interface, which is 1080 $Å^2$ larger in Cfl2 than in Cfl1 and has a substantially more favorable predicted binding energy. Given this striking difference, we also analyzed the corresponding Cif and aCif dimer interfaces. We found that the surface area of the canonical dimer interface of Cfl2 is very similar to those of Cif and aCif, albeit with a modestly higher contribution from hydrophobic residues; the Cfl1 dimer interface is markedly smaller than all of the others (Table 2).

We hypothesized that the large difference between Cfl1's canonical dimerization surface area and energetics and those of Cfl2, Cif, and aCif would allow for more intra-dimer flexibility for Cfl1. In order to test this hypothesis, we carried out Normal Mode Analysis (NMA) to observe the large-scale, longer time-regime movements available for each dimer. In the case of Cfl1 and Cfl2, the dimers were extracted from their respective oligomers before doing the analysis. Unsurprisingly, a comparison of the first non-trivial mode of each dimer shows that the Cfl1 dimer exhibits the largest excursions (Supplementary Movie 1).

Supplementary video related to this article can be found at https://doi.org/10.1016/j.crstbi.2021.02.002

In contrast to the relative looseness of the Cfl1 canonical dimer interface, we found that the total area of all the oligomeric interfaces in Cfl1 is 435 $Å^2$ larger than the total area of the corresponding interfaces in Cfl2 (Table 2). When comparing the Cfl1 and Cfl2 structures more closely, we observed that the close-contact (<3.2 Å) interactions at their oligomerization interfaces are organized in three similar "clusters" (Fig. 7, insets). Clusters 1 and 2 are both part of the in-ring interfaces [*i.e.*, 1:3 and 1:7 (Cfl1) or 1:9 (Cfl2)], while cluster 3 is part of the cross-ring (*i.e.*, 1:4) diagonal interface. Cluster 1 is where the N-terminus of one monomer contacts the neighboring monomer. In the case of Cfl1, monomer 1 interacts with the N-terminus of adjacent monomer 3, but in Cfl2 the opposite is true: monomer 3 interacts with the N-terminus of monomer 1 (Fig. 7(A) and (D), cluster 1; Fig. S3(A) and (B)). The different oligomerization states of the two structures coincide not only with different N-terminal donor-acceptor relationships among neighboring monomers within each ring, but also with different conformations of the monomers in the dimer subunit across each ring (Fig. S3(C) and S3(D)). The N-terminus of Cfl1 monomer 3 makes several electrostatic interactions with monomer 1, as well as a hydrophobic interaction mediated by the insertion of Met13 into a pocket comprised of Phe22, Phe26, Val41, Trp61, and the hydrocarbon portions of Glu23 and Arg28 side chains (Fig. 7(A), cluster 1). Similarly, in Cfl2, the N-terminus of monomer 1 makes several electrostatic interactions with monomer 3 and a hydrophobic interaction between Pro17 and Tyr287 (Fig. 7(D), cluster

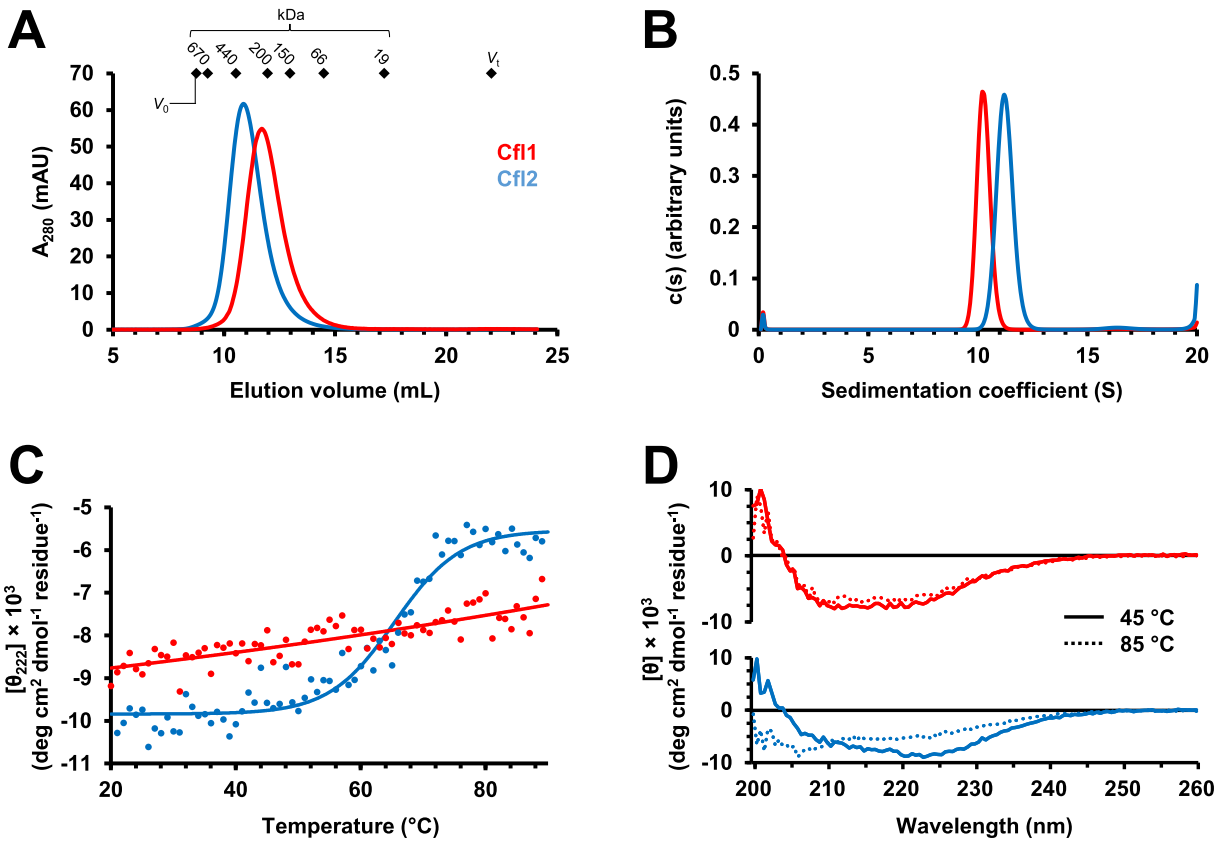

Fig. 3. Biochemical characterization of Cfl1 and Cfl2. (A) Cfl1 (red) and Cfl2 (blue) elute as large oligomers in SEC. Diamonds indicate the Superdex S200 10/30 column void volume (V_0), total volume (V_t), and peak elution volumes of molecular mass standards (670 kDa = bovine thyroglobulin, 440 kDa = equine spleen apoferritin, 200 kDa = sweet potato β-amylase, 150 kDa = yeast alcohol dehydrogenase, 66 kDa = bovine serum albumin, 19 kDa = bovine carbonic anhydrase). (B) Sedimentation coefficient distribution of Cfl1 (red) and Cfl2 (blue) analyzed by velocity sedimentation analytical ultracentrifugation. (C) Molar ellipticity at 222 nm (θ_{222}) was monitored as Cfl1 (red) and Cfl2 (blue) were heated to determine their melting temperatures (n = 1) Solid lines represent linear (Cfl1) or logistic (Cfl2) fits to the observed data. (D) Molar ellipticities of Cfl1 (red; top panel) and Cfl2 (blue; bottom panel) between 200 and 260 nm are shown at 45 °C (solid lines) and 85 °C (dashed lines). (For interpretation of the references to colour in this figure legend, the reader is referred to the web version of this article.)

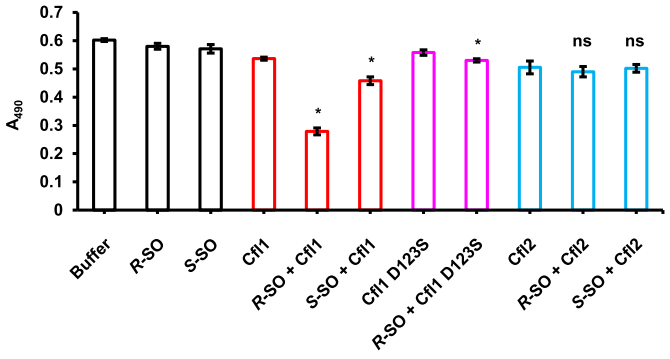

Fig. 4. Cfl1 is an active epoxide hydrolase. Cfl1 (red) and Cfl2 (blue) catalytic activity against the *R* and *S* enantiomers of styrene oxide (SO) and the catalytic activity of Cfl1-D123S (magenta) against *R*–SO was determined using the adrenochrome end-point assay. A decrease in absorbance at 490 nm indicates hydrolysis of the epoxide. Values are reported as the means of three experiments, and the error bars represent the standard deviations. Buffer and substrate-only controls are shown in grey. An asterisk indicates $p < 0.05$ when Student's unpaired *t*-test was used to compare the protein + substrate reactions and their respective protein-only controls (n = 3). ns, not signficant. (For interpretation of the references to colour in this figure legend, the reader is referred to the web version of this article.)

1). Cluster 2 is located near Cluster 1 in both structures but does not involve the N-terminus (Fig. 7(A) and (D), cluster 2). Lastly, Cluster 3 is where monomer 1 contacts monomer 4, and is the only point of contact between these two monomers in both structures (Fig. 7(B) and (D), cluster 3).

Finally, we sought to confirm that the sharp decrease in the activity of Cfl1-D123S seen in Fig. 4 is not due to a gross change in the overall structure of the enzyme or its active site caused by the single amino-acid substitution. To that end, we determined the crystal structure of Cfl1-D123S. Data were obtained to 2.15 Å resolution (Table 1), although the UCLA Diffraction Anisotropy Server reports modest anisotropy (2.2, 2.5, and 2.3 Å along **a***, **b***, and **c***, respectively) (Strong et al., 2006). As a result, we refined translation, libration, and screw (TLS) rotation parameters (Schomaker and Trueblood, 1968), which created a significant improvement in the R_{free} value without overfitting, as judged by R_{free}-R_{work}. As shown in Fig. S4, the RMSD of main-chain atoms between wild-type Cfl1 and Cfl1-D123S monomers is 0.2 Å. Closer inspection of the mutant enzyme's active site shows that, apart from the D123S substitution, the active site is largely unchanged compared to the wild-type enzyme (Fig. S4, inset).

2.6. Evolutionary conservation of the Cfl1 and Cfl2 interfaces

Given the novel oligomerization interfaces of Cfl1 and Cfl2 in comparison to other structurally characterized members of the α/β hydrolase superfamily, we were interested in examining the evolutionary conservation of the oligomer interfaces among homologs and how they compare to the canonical dimer interfaces. We used the ConSurf server to analyze the sequence conservation of Cfl1 and Cfl2 (Ashkenazy et al., 2016; Landau et al., 2005).

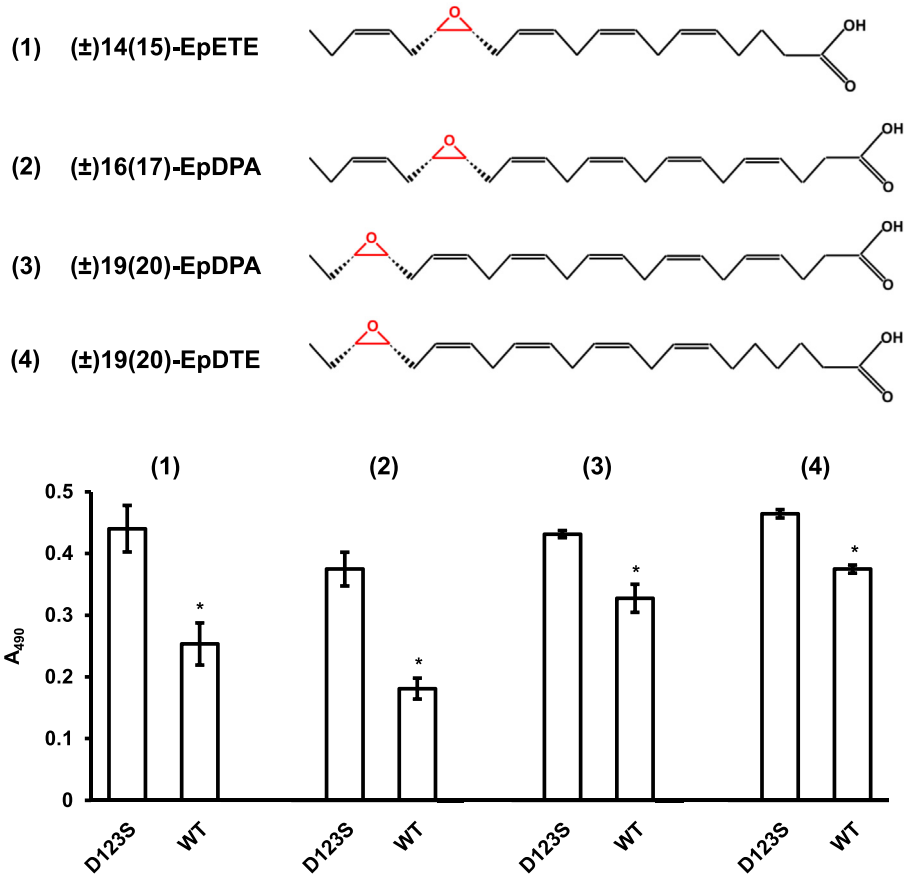

Fig. 5. Cfl1 hydrolyzes physiological epoxides *in vitro*. Top: The structures of four physiological epoxides (1–4) are shown. The epoxide moiety is highlighted in red. Bottom: the hydrolysis activity of Cfl1-D123S and Cfl1-WT is shown for each of the four physiological epoxides as determined by the adrenochrome end-point assay. Values are reported as the means of three experiments, and the error bars represent the standard deviation. An asterisk indicates $p < 0.05$ when Student's unpaired *t*-test was used to compare the wild-type enzyme reactions to D123S mutant controls for a particular substrate (n = 3). (For interpretation of the references to colour in this figure legend, the reader is referred to the web version of this article.)

Comparing the average conservation scores of the interfaces' surface residues reveals that the Cfl1 dimer interface is more conserved than its higher-order oligomeric interfaces, while the Cfl2 dimer interface, as a whole, is less well-conserved and does not appear to be the most conserved interface (Table S2). Residues in both dimer interfaces are more conserved on average than the non-interface surface residues of their respective proteins (Table S2). We note that these differences in the means are not statistically significant due to relatively large standard deviations of conservation scores across whole interfaces. Indeed, comparing the local conservation pattern between the interfaces reveals interesting differences between the dimer interfaces and the oligomer interfaces of both proteins (Fig. 8). Both Cfl1 and Cfl2 1:2 interfaces contain a central, relatively larger area of high conservation that is lacking in their oligomeric interfaces. This qualitative difference remains largely true even when we excluded non-Cif-like homologs from the analysis (Fig. S5). When we analyzed the equivalent 1:2 interfaces of Cif and aCif, we found a similarly positioned and conserved "pivot point" in both dimer interfaces (Fig. 8). These data suggest that a portion of the dimer interfaces may have evolved before the oligomer interfaces, and that the dimer interface may be under evolutionary pressure to serve a different function than the oligomer interfaces. The least sequence conservation is observed at the Cfl1 1:7 and Cfl2 1:9 interfaces (Fig. 8 and Table S2).

Although the dimer interfaces of all four proteins feature a central pivot point that is highly conserved, this region is also surrounded by more polymorphic residues in all cases (Fig. 8). One such polymorphic patch found in Cif and Cfl2 is missing from Cfl1's interface (Fig. 8, red dashed box). The absence of this region in Cfl1 is a major reason that its dimer interface surface area is smaller compared to those of Cfl2, Cif, and aCif. The same area in aCif shows above-average conservation, but remains less conserved than the core of the interface (Fig. 8). Along with NMA results showing that the isolated Cfl1 dimer is the most flexible of the four, these data suggest that the dimer interfaces retain a central conserved pivot point with the surrounding polymorphic region serving as a modifier of inter-dimer flexibility according to functional needs.

3. Discussion

Structural flexibility can be a critical factor in enzymatic catalysis. Flexibility plays an important role in substrate specificity and turnover, and it is perhaps especially important for enzymes in which two or more domains contribute to the active-site architecture (Pintar et al., 2020; Light et al., 2017). Indeed, protein scientists have learned from nature to leverage this principle and manipulate enzyme dynamics to create new functionalities (Boehr et al., 2018). Although an experimental relationship between the structural dynamics of epoxide hydrolyses and their catalytic activity is yet to be established, work on the fluoroacetate dehalogenase (FAcD) from *Rhodopseudomonas palustris*, a dimeric enzyme closely related to the Cif-like epoxide hydrolases, has shown that intra- and inter-monomer dynamics are coupled to the catalytic cycle of the enzyme (Kim et al., 2017; Mehrabi et al., 2019a, 2019b). With alignment of FAcD monomer main-chain atoms versus Cfl1 or Cfl2 resulting in RMSD of less than 1 Å (data not shown), it is reasonable to suspect that the activity of Cfl1 and Cfl2 could also be influenced by protomer dynamics.

Despite some similarities between the two structures, the steric environments of the Cfl1 and Cfl2 monomers are distinct and likely lead to differences in freedom of motion. The key differences we noted include the N-terminus donor-acceptor relationships between the monomers, the surface areas and binding energies of the interfaces, and the conformations of the dimer subunit in each structure. Comparative NMA between the dimers of Cfl1, Cfl2, Cif, aCif showed that the *ex circulum* (*i.e.*, out of the ring) dimer of Cfl1 with its smallest dimer interface is the most flexible (Supplemental Movie 1). However, within the ring, several

Table 1
Data collection, reduction, and refinement statistics.

Data collection & reduction	Cfl2	Cfl1-WT	Cfl1-D123S
Beamline	SSRL 14-1	NSLS-II 17-ID-1	NSLS-II 17-ID-1
Wavelength (Å)	1.1808	0.9793	0.9201
Space group	$P\,2_1\,2_1\,2$	$I\,4\,2\,2$	$C\,2$
Unit cell parameters:			
a, *b*, *c* (Å)	182.7, 210.5, 87.0	132.2, 132.2, 341.7	195, 98.4, 170
α, β, γ (°)	90, 90, 90	90, 90, 90	90, 118.6, 90
Resolution[a] (Å)	46.9–2.2 (2.33–2.2)	45.8–2.2 (2.33–2.2)	44.7–2.15 (2.25–2.15)[g]
R_{meas}[b] (%)	9.7 (84.1)	17.8 (138.7)	9.3 (101.2)
$CC_{½}$[c] (%)	99.9 (82.2)	99.8 (79.4)	99.8 (73.1)
I/σ_I	16.6 (2.45)	11.71 (1.97)	10.66 (1.46)
Completeness (%)	99.9 (99.8)	99.5 (96.9)	99.0 (94.8)
Redundancy	7.5 (7.47)	13.3 (13.4)	3.5 (3.6)
Refinement			
Total number of reflections	170263	76600	152005
Reflections in the test set	8500	3819	7615
R_{work}[d]/R_{free}[e] (%)	18.59/21.60	18.20/21.38	20.89/23.97
Number of atoms:			
Protein	23337	9276	18502
Water	1141	604	787
Ramachandran plot[f] (%)	97.4/2.6/0.0	96.8/2.9/0.3	96.8/2.8/0.3
$B_{average}$ (Å^2):			
Protein	39.3	42.1	57.5
Water	41.6	44.5	45.6
Bond length RMSD (Å)	0.01	0.01	0.01
Bond angle RMSD (°)	1.13	1.05	1.10
PDB ID	7JQZ	7JQX	7JQY

[a] Values in parentheses correspond to the highest resolution shell.
[b] R_{meas}: the redundancy independent R-factor, described in Diederichs and Karplus (1997); Nat. Struct. Biol. 4, 269–275.
[c] $CC_{½}$: the percentage of correlation between intensities from random half-datasets, described in detail in Karplus and Diederichs (2012); Science 336, 1030–1033.
[d] $R_{work} = \Sigma_h\,|F_{obs}(h) - F_{calc}(h)|/\Sigma_h\,F_{obs}(h)$, $h \in$ {working set}.
[e] $R_{free} = \Sigma_h\,|F_{obs}(h) - F_{calc}(h)|/\Sigma_h\,F_{obs}(h)$, $h \in$ {test set}.
[f] Favored/allowed/outliers.
[g] The data are moderately anisotropic.

factors may act together to further differentiate the steric environment of the Cfl1 monomer from that of Cfl2, and the difference in the dimer interface is but one of them.

Further analysis of the first three non-trivial normal modes of the four proteins reveals that the Cif and aCif dimer motions are coupled to extensive intra-monomer deformations, specifically between the core and cap domains (Fig. 9). Compared to Cif and aCif, the extracted Cfl1 dimer deformations are concentrated in a much smaller footprint (Fig. 9, "*ex circulum*"). While the dimer interface is smaller in Cfl1, the interfaces formed during its further oligomerization are actually somewhat more extensive than the interfaces formed by Cfl2 (delta = +435 Å^2), but not to an extent that compensates fully (Table 2). As a result, within the Cfl1 ring, the three dominant modes include interdimer flexion, seen in the form of new areas of deformation which correspond to its oligomer interfaces that are lacking from the *ex circulum* Cfl1 dimer (Fig. 9, bottom row). This is not the case with Cfl2, where the *ex circulum* dimer loses its deformability at the dimer interface once it oligomerizes but the oligomer interface deformations do not compensate to the same degree as they do in Cfl1 (Fig. 9, bottom row). Correspondingly, within the ring, Cfl1 retains some flexibility at the dimer interface, whereas Cfl2 appears more tightly constrained.

These observations suggest that the Cfl1 and Cfl2 rings offer different degrees of flexibility for their respective dimers. We hypothesize that Cfl1, but not Cfl2, retains sufficient intra-monomer flexibility *in circulum* to achieve substantial catalytic activity. Additionally, we speculate that dissociation or loosening of the ring may modulate the activity of each protein.

Interface conservation analysis suggests that the higher-order oligomeric interfaces of Cfl1 and Cfl2 may have evolved after the canonical dimer interfaces that they share with Cif and aCif. In addition to the aforementioned steric influence of these assemblies on the activity of their respective subunits, the novel dihedral point-group symmetries of Cfl1 and Cfl2 may also indicate a divergent biological function compared to C_2-symmetric Cif and aCif. Indeed, by examining the relative enrichment of gene ontology (GO) annotation terms associated with proteins with different symmetry types, Bergendahl and Marsh have shown that dihedral homomers are strongly associated with metabolic processes, whereas proteins with C_2 symmetry are enriched in GO terms associated with binding and processing of small molecules (Bergendahl and Marsh, 2017). And as metabolic processes often require fine-tuning of enzymatic activity, the added oligomer interfaces of Cfl1 and Cfl2 could theoretically allow for more sophisticated cooperative behaviors, such as simultaneous positive and negative cooperativity, which would not be possible in a dimer (Vivoli et al., 2017). Ultimately, a better understanding of the evolution of these oligomer interfaces would be served by mutagenesis and functional analysis, together with experiments to elucidate the biological functions of Cfl1 and Cfl2 through *in vivo* experiments (e.g., gene knock-outs). Such experiments may also provide more biological context to the puzzling observation that transcription of *cfl2*, not *cfl1*, is increased in response to epoxide stimulus.

The involvement of the N-termini in forming the oligomer interfaces of Cfl1 and Cfl2 represents an extension of the known functions of the N-termini in α/β epoxide hydrolases. In aCif, the N-terminus forms an α-helix on the side of the protein opposite the active site, and then contacts the active-site entry by wrapping around the dimer interface as an unstructured loop, forming monomer-monomer interactions along the way (Bahl et al., 2014). Interestingly, the position of the aCif monomer-monomer contacts mediated by the N-termini resembles that of the 1:4 (Cluster 3) interface contact in Cfl1 and Cfl2. *Aspergillus niger* epoxide hydrolase has a long N-terminus extension which forms a "meander" that also participates in the dimer-interface contacts (Zou et al., 2000). These similarities suggest a possibly more general role for the N-terminus in stabilizing monomer-monomer interactions in some α/β epoxide hydrolases.

B. cenocepacia can establish a presence in a diversity of microenvironments, ranging from the soil to the human lung, where the epoxide hydrolysis of Cfl1 may be deployed. Cfl1 may detoxify xenobiotic epoxides encountered by *B. cenocepacia* in these environments, or funnel them as an energy source in a manner similar to other microorganisms (Bendigiri et al., 2017; Jacobs et al., 1991). In addition to xenobiotic epoxides, we found that Cfl1 can hydrolyze human-derived epoxides. This raises the possibility that *B. cenocepacia* may potentially utilize Cfl1 in a manner similar to *P. aeruginosa*, which uses Cif to sabotage host signaling pathways. Although Cif's ability to be secreted presumably aids in its capacity to encounter and hydrolyze host epoxides during an infection, it is unknown if secretion is a requirement, as some fatty acids are able to diffuse passively through the membrane (Kamp and Hamilton, 2006). Cfl1 is predicted to lack general secretory pathway (Sec) and twin-arginine translocation (TAT) motifs. However, there have been instances in the literature of proteins that lack a strict TAT motif, yet are secreted through this pathway directly or indirectly (Hinsley et al., 2001; Ignatova et al., 2002; Rodrigue et al., 1999).

The lack of substantial Cfl2 activity raises the possibility that it may function as a non-catalytic pseudoenzyme *in vivo*. Pseudoenzymes are typically classified as such based on sequence analyses that reveal missing critical catalytic residues. However, this is not the case with Cfl2, which maintains the epoxide hydrolase motifs in its amino acid sequence and 3-dimensional arrangement of its catalytic residues. A previous study by van Loo *et al.* found that four out of twelve predicted bacterial epoxide hydrolases that they expressed in soluble form showed very low

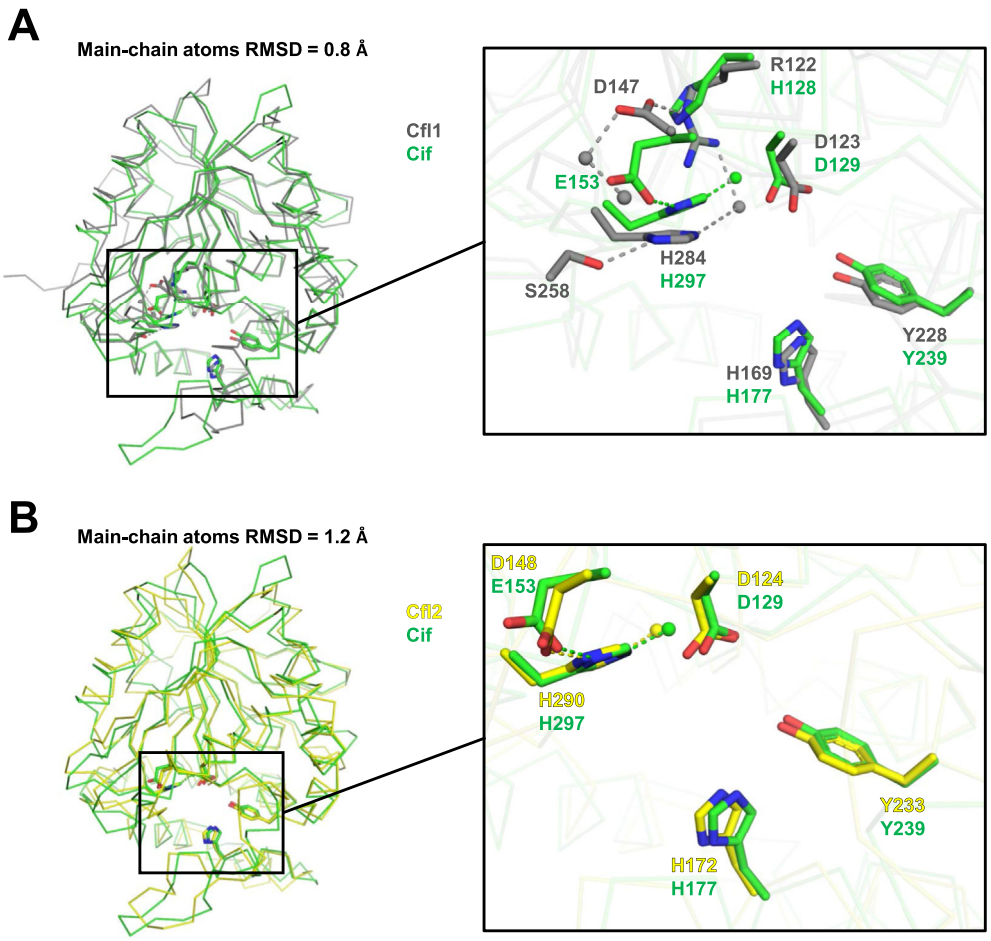

Fig. 6. Alignment of the Cfl1 and Cfl2 monomers to the Cif monomer. The main-chain atoms of the Cif (green) and Cfl1 (grey) (A), and of Cif and Cfl2 (yellow) (B) monomers aligned using PyMol are shown. The insets show a closer view of the catalytic and other select active-site residues (sticks) and waters (spheres). Electrostatic and hydrogen-bond interactions are represented as dashed lines. (For interpretation of the references to colour in this figure legend, the reader is referred to the web version of this article.)

hydrolysis activity against the 25-substrate panel they tested (van Loo et al., 2006). As the number of biochemical studies of epoxide hydrolases continues to accumulate, sequence analyses paired with structural comparisons may allow us to fine-tune the criteria for differentiating between active and pseudo-epoxide hydrolases.

4. Materials and Methods

4.1. RT-qPCR

B. cenocepacia strain HI2424 was streaked on an lysogeny broth (LB (Bertani, 1951);) agar plate and incubated overnight at 37 °C. Several colonies were used to inoculate a 5 mL LB broth and grown overnight at 37 °C in a rotary incubator. Fifty microliters of the overnight culture was used to inoculate 5 mL of LB broth containing 0.02% DMSO [(*v*/*v*), = 2.8 mM], 1 mM of EBH, *R*–SO, or *S*–SO. When each culture reached an $O.D._{600}$ of 1.0, 1 mL of culture was spun down at 3000×*g*, 4 °C, for 10 min and the pellet was stored at −80 °C. RNA was extracted from thawed pellets using the RNeasy RNA extraction kit (Qiagen), and genomic DNA was digested using the RQ1 kit (Promega). cDNA was generated using qScript® cDNA SuperMix (Quantabio) and stored at −20 °C. RT-qPCR was performed using PerfeCTa® SYBR® Green FastMix® for iQ™. "No-template" and "extracted RNA template" RT-qPCR reactions were included as negative controls for genomic DNA contamination. Genomic DNA from *B. cenocepacia* strain HI2424 was used to generate a standard curve for each pair of primers.

4.2. Cloning, protein expression, and purification

Cfl1 (accession number ABK11134.1) and Cfl2 (accession number ABK10685.1) from *B. cenocepacia* strain HI2424 and Cfl1 from *B. cenocepacia* strain K56-2 (EPZ88246.1, 100% amino acid identity to CAR55383.1 from strain J2315) coding sequences were PCR amplified and inserted into pCDB24 digested with Xho1 using Gibson Assembly. BL21(DE3) cells were transformed with plasmid and grown on LB + 100 μg/mL carbenicillin agar plates at 37 °C overnight. One transformed colony was used to inoculate 10 mL of LB + 100 μg/mL carbenicillin broth and grown overnight at 37 °C. After ~12 h, the overnight culture was used to inoculate 1 L of Terrific Broth (Tartoff and Hobbs, 1987) in a 2 L baffled flask and allowed to grow at 37 °C with shaking at 180 rpm. When the culture reached an $O.D._{600}$ of ~0.3, the bacteria were moved to 16 °C with shaking at 180 rpm for 1 h. Expression was then induced with 0.1 mM isopropyl β-D-1-thiogalactopyranoside. After ~24 h of expression, the bacteria were spun down at 5250×*g* for 30 min at 4 °C. The supernatant was discarded and the pellet was resuspended in lysis buffer (500 mM NaCl, 20 mM Tris, pH 8.5, 40 mM imidazole, pH 8.5, 2 mM $MgCl_2$) supplemented with 25 units/mL of Pierce Universal Nuclease. Cells lysis was carried out using an M-110L microfluidizer (Microfluidics) in 3 passes at ~18 kpsi. The cell lysate was spun down at 40,000 rpm in a Type 45 Ti rotor for 1 h at 4 °C, and the supernatant was filtered through a 0.45 μm MCE membrane (Millipore) to remove residual cell debris. Five milliliters of HisPur Ni-NTA resin (Thermo Fisher Scientific) washed with 50 mL of equilibration buffer (500 mM NaCl, 20 mM Tris, pH 8.5, 40 mM imidazole, pH 8.5) were added to the clarified cell lysate, and the mixture was gently stirred at room temperature for 30 min. The mixture of resin and clarified lysate was then passed through a gravity column. The protein-bound resin was washed with 50 mL of equilibration buffer followed by two 50 mL washes with 500 mM NaCl, 20 mM Tris, pH 8.5, 100 mM imidazole, pH 8.5. The protein was then eluted in 50 mL of 500 mM NaCl, 20 mM Tris, pH 8.5, 500 mM imidazole, pH 8.5. The eluate was supplemented with 5.6 mL of 10 × Ulp1 reaction buffer (1.5 M NaCl, 500 mM Tris, pH 8.5, 10 mM DTT, 2% [*v*/*v*] IGEPAL CA-630) and 1.2 mg of Ulp1 protease. The cleavage reaction was simultaneously dialyzed overnight against 4 L of 20 mM NaCl, 20 mM Tris, pH 8.5, 0.5 mM

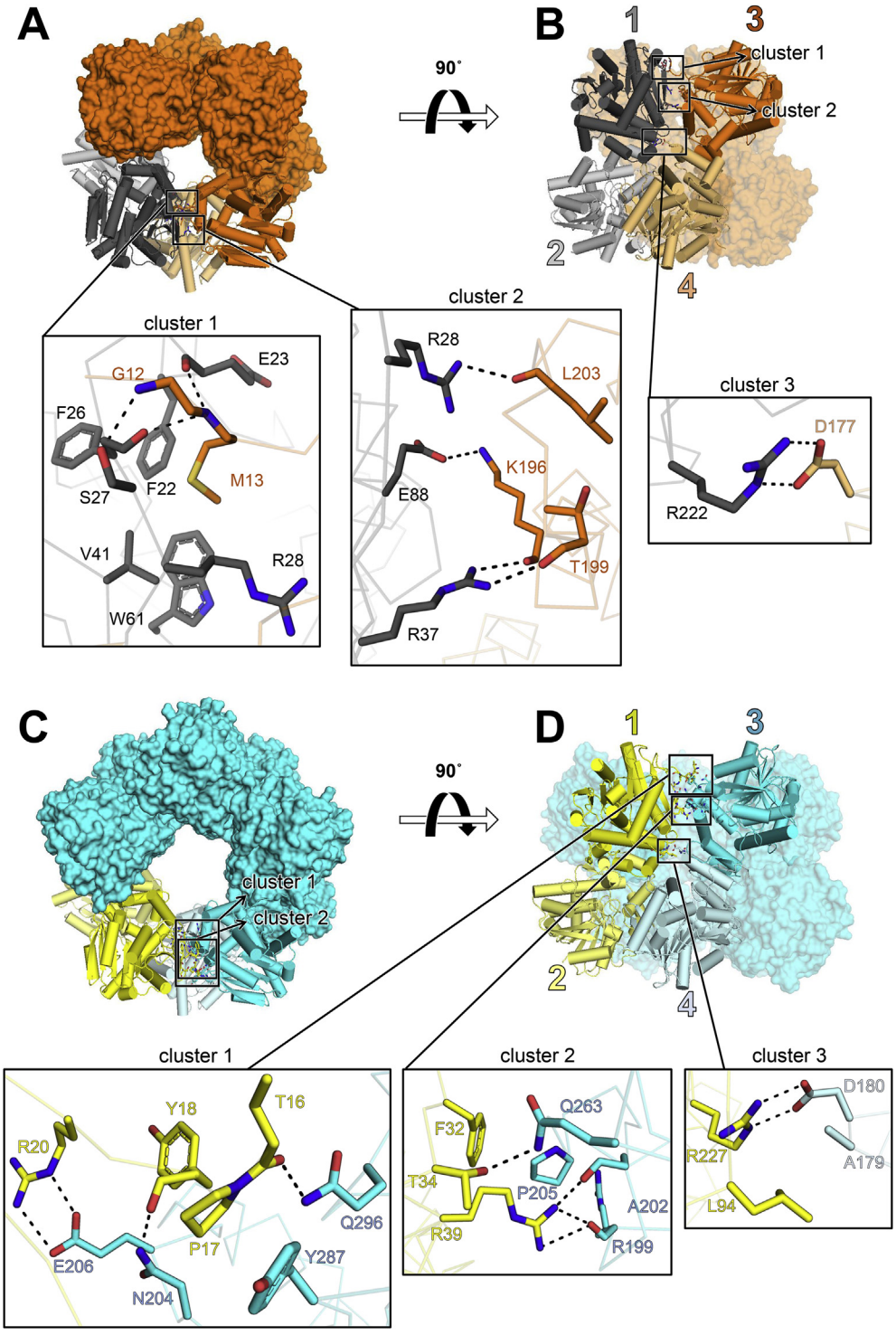

Fig. 7. Crystal structures of Cfl1 and Cfl2. (A) Top view of Cfl1. All subunits are shown in surface representation except subunits 1–4, which are shown in cartoon representation with cylindrical α-helices. All subunits are colored orange except dimer subunits 1 and 2, which are highlighted in grey. (B) Side view of Cfl1. Colors and representations are the same as in (A). Subunits 1–4 are numbered. The positions of Cluster 1 and Cluster 2 in this perspective are only outlined with boxes. (C) Top-down view of Cfl2. All subunits are shown in surface representation except subunits 1–4, which are shown in cartoon representation with cylindrical α-helices. All subunits are colored cyan except dimer subunits 1 and 2, which are highlighted in yellow. The positions of Cluster 1 and Cluster 2 in this perspective are outlined with boxes. (D) Side view of Cfl2. Colors and representations are the same as in (C). Subunits 1–4 are numbered. Subunits 7 (Cfl1) and 9 (Cfl2) are adjacent to subunit 1, closing the ring on the opposite side from subunit 3. Insets represent magnified views of clusters 1–3 in each structure. Side chains are depicted as sticks and electrostatic interactions as dashes. Main-chain atoms involved in electrostatic interactions are depicted as sticks; otherwise they are shown as transparent ribbons. Oxygens are colored red, and nitrogens are colored blue. (For interpretation of the references to colour in this figure legend, the reader is referred to the web version of this article.)

TCEP-HCl at room temperature. The cleaved protein was then passed through HisPur Ni-NTA resin equilibrated with 20 mM NaCl, 20 mM Tris, pH 8.5, 5 mM imidazole, pH 8.5. The flow-through was then applied to a HiTrap Q HP 5 mL anion exchange chromatography column (GE Healthcare) attached to an ÄKTA Explorer 100 system (Amersham Pharmacia Biotech). The protein was eluted using a 200 mL gradient of wash buffer (20 mM NaCl, 20 mM Tris, pH 8.5) and increasing concentration of elution buffer (1 M NaCl, 20 mM Tris, pH 8.5) (Lau et al., 2018).

4.3. Hydrodynamic analysis

A Superdex 200 10/300 SEC column (Amersham Pharmacia Biotech) attached to an ÄKTA FPLC system (Amersham Pharmacia Biotech) was used to obtain peak elution volumes for Cfl1, Cfl2, and SEC standards (Sigma Aldrich). Column equilibration and sample elution were carried out at 4 °C using 150 mM NaCl, 50 mM sodium phosphate pH 7.4, and 0.02% (*w/v*) NaN_3 at a flow-rate of 0.5 mL/min. The diffusion coefficients (D) of Cfl1 and Cfl2 were extrapolated from the plot of the partition coefficients (K_{av}) of the standards versus their known diffusion coefficients.

Velocity sedimentation analytical ultracentrifugation was carried out using 7 μM of Cfl1 and 8 μM of Cfl2 in a ProteomeLab XL-A centrifuge (Beckman Coulter) at 25,000 rpm, 20 °C, in an An-60 Ti rotor. Sample sedimentation was monitored through absorbance at 280 nm. Data were analyzed using SEDFIT (15.01b) and SEDNTERP (20120828 BETA) to obtain the sedimentation coefficients (Schuck, 2000; Laue et al., 1992). The relative molar masses of Cfl1 and Cfl2 were estimated using the

Table 2
Rosetta analysis of the interfaces of Cfls and Cifs.

interface[a]	buried surface area (Å^2)	% nonpolar buried surface area	% polar buried surface area	shape complementarity	$\Delta\Delta G$ (kcal/mol)
Cfl1 1:2	1471	80	20	0.67	−21.5
Cfl1 1:3	1095	59	41	0.69	−36.4
Cfl1 1:4	971	71	29	0.59	−25.8
Cfl1 1:7	1113	58	42	0.70	−39.0
Cfl2 1:2	2551	85	15	0.70	−80.4
Cfl2 1:3	989	49	51	0.65	−19.3
Cfl2 1:4	694	67	33	0.71	−23.0
Cfl2 1:9	1061	46	54	0.67	−31.6
Cif 1:2	2685	76	24	0.75	−63.1
aCif 1:2	2983	68	32	0.76	−84.5

[a] The interface interactions are numbered according to the monomer numbering in Fig. 7.

Svedberg equation:

$$M = \frac{sRT}{D(1 - \bar{v} \cdot \rho)}$$

where M is the relative molar mass of the protein in g/mol, s is the sedimentation coefficient of the protein in Svedbergs (10^{-13} s), R is the gas constant in J/mol/K, T is the temperature in K, D is the diffusion coefficient of the protein in cm^2/sec, $\bar{v}$ is the partial specific volume of the protein in mL/g, and ρ is the buffer density in g/mL.

4.4. Circular dichroism spectroscopy

Circular dichroism spectroscopy was performed using a JASCO J-815 spectrometer equipped with a CDF-426S Peltier temperature controller and a 5 mm-pathlength quartz cuvette. Circular dichroism was monitored at 222 nm for a buffer-only sample (20 mM sodium phosphate, pH 7.4) and 1.5 μM Cfl1 or Cfl2 samples while the temperature was increased from 20 to 90 °C in 1 °C increments with a 5-s period of equilibration and a 1-s integration time for each measurement. The same equipment and sample conditions were used to acquire wavelength scans from 200 to 260 nm while monitoring circular dichroism from three accumulations with a 1-s integration time following equilibration at temperatures of 45 °C and again at 85 °C. The raw data of the buffer-only sample were subtracted from the raw data of the protein samples before converting them to and plotting them in molar ellipticity units in Excel.

4.5. Epoxide hydrolysis assay

An adrenochrome reporter end-point assay adapted from Cedrone et al.

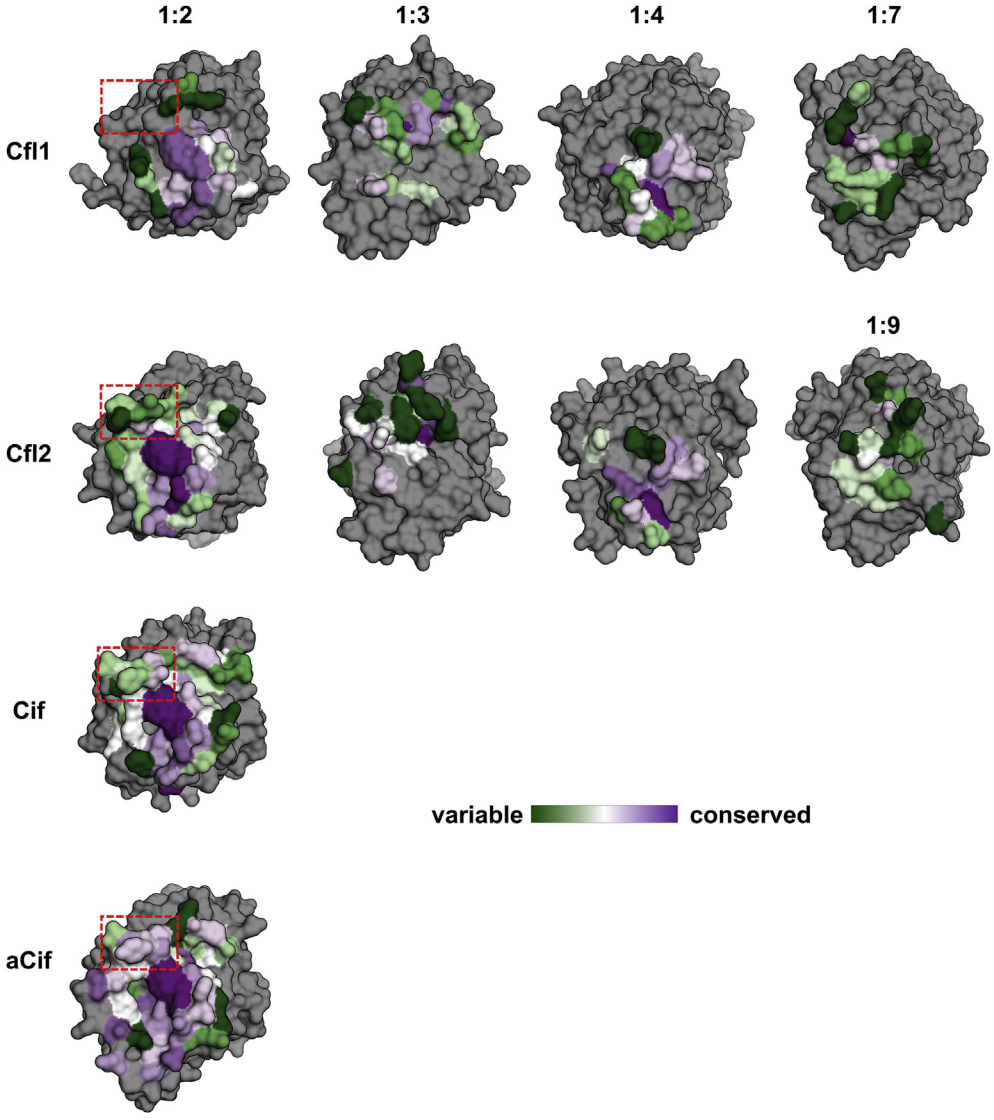

Fig. 8. Evolutionary conservation of the interfaces of the Cfls and Cifs. The interfaces of Cfl1, Cfl2, Cif, and aCif are shown on each protein's monomer subunit as surfaces. The interfaces are labeled at the top according to the monomer numbering described in Fig. 7. The interface residues calculated by Rosetta are colored according to the ConSurf conservation score as indicated by the color legend, and all other residues are colored grey. The regions outlined with red dashed boxes indicate a structural element that is found in Cfl2, Cif, aCif, but not Cfl1. (For interpretation of the references to colour in this figure legend, the reader is referred to the web version of this article.)

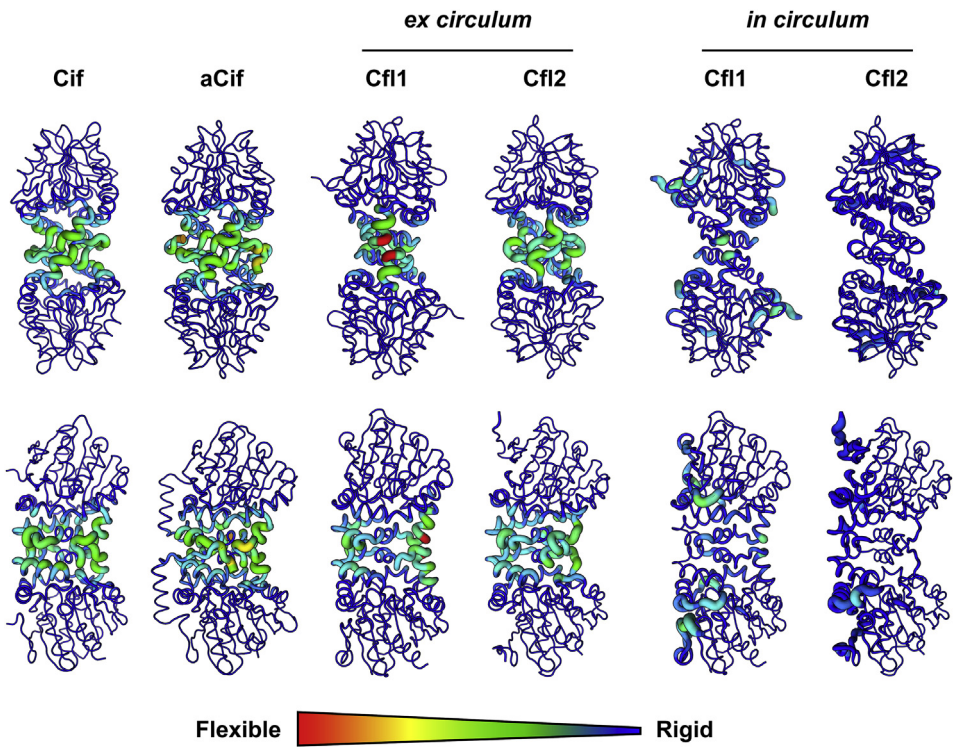

Fig. 9. Deformation energy analysis of the Cfls and Cifs. The sum of the deformation energies of the first three modes of each protein is depicted as a heatmap onto its structure. The colors and thickness of the heatmap indicate relative flexibility and rigidity as shown by the scale. The top row shows the face-on view of each dimer, and the bottom row shows the side-on view. In the case of the "*ex circulum*" (out of the ring) Cfl1 and Cfl2 dimers, the calculations were performed on the dimer after extracting it from its respective oligomer. *in circulum*, in the ring. (For interpretation of the references to colour in this figure legend, the reader is referred to the web version of this article.)

was used to measure the relative amount of hydrolyzed epoxide (Cedrone et al., 2005). Absorbance at 490 nm was measured using a TECAN Infinite M1000 reader or a Biotek Synergy Neo2 reader. All reactions were carried out at 37 °C with 20 μM protein and 2 mM substrate in 100 mM NaCl, 20 mM HEPES, pH 7.4, and 2% DMSO. When testing the activity of Cfl2 against biological substrates, 80 μM protein was used. The xenobiotic epoxide reactions proceeded for 1 h in a 100 μL reaction, and the poly-unsaturated fatty acid epoxide reactions proceeded for 2 h in a 50 μL reaction. The reactions were quenched by adding 0.5 × the starting reaction volume of a solution of 90% acetonitrile containing sodium periodate at a 1:1 M ratio to the starting substrate and incubating for 30 min at room temperature. A molar excess of epinephrine-HCl in 0.5 × the starting reaction volume was finally added, and an aliquot of 100 μL (xenobiotic epoxide reactions) or 90 μL (fatty acid epoxide reactions) was then used to measure absorbance at 490 nm in a transparent 96-well flat-bottom plate. Replicates for each experiment were obtained by performing the hydrolysis reactions on different days using the same preparation of each enzyme and making new enzyme and substrate working stocks for each replicate.

4.6. Electron microscopy

Using a 400-mesh carbon-coated (4–6 μm thick) copper grid that was glow discharged for 30 s at 20 mA in residual air, a 5 μL aliquot of Cfl2 at a concentration of 10 μg/mL in 100 mM NaCl, 20 mM HEPES, pH 7.4 was applied to the grid for 30 s. The solution was then quickly blotted with filter paper, briefly washed with 5 μL of buffer and blotted, and then stained with 5 μL of 0.75% (*w/v*) uranyl formate, blotted, and then left to air dry. Images were acquired on an FEI Tecnai F20ST microscope with a Gatan OneView camera. Reference-free class averages of 800 manually picked particles were generated using EMAN2 (Tang et al., 2007).

4.7. Crystallography

Cfl2 crystals were obtained in a hanging drop composed of 2 μL of 1.5 mg/mL protein in 20 mM NaCl, 10 mM HEPES pH 7.5 and 2 μL of well solution (784 mM sodium thiocyanate, 12% [*w/v*] PEG 3350) and equilibrated by vapor diffusion against 400 μL of well solution. The harvested crystals were soaked in cryoprotectant solution (20% [*v/v*] ethylene glycol, 800 mM sodium thiocyanate, 14% [*w/v*] PEG 3350) before flash cooling in liquid nitrogen. The oscillation data collection was performed at the Stanford Synchrotron Radiation Lightsource beamline 14-1 equipped with a MAR325 detector at 100 K, an oscillation range of 0.3° per frame, a total of wedge of 180°, and a wavelength of 1.18076 Å. Wild-type Cfl1 crystals were obtained in a hanging drop composed of 2 μL of 5.2 mg/mL protein in 20 mM NaCl, 20 mM HEPES pH 7.4 and 2 μL of well solution (750 mM potassium sodium tartrate, 100 mM HEPES pH 8.1) and equilibrated by vapor diffusion against 400 μL of well solution. The harvested crystals were directly flash cooled in liquid nitrogen without further cryoprotection. The oscillation data collection was performed at the National Synchrotron Light Source II beamline 17-ID-1 (AMX) equipped with an Eiger 9M detector at 100 K, an oscillation range of 0.1° per frame, a total of wedge of 180°, and a wavelength of 0.979331 Å. Cfl1-D123S crystals were obtained in a hanging drop composed of 2 μL of 1.9 mg/mL protein in 20 mM NaCl, 20 mM HEPES pH 7.4 and 2 μL of well solution (6% [*v/v*] ethylene glycol, 8% [*w/v*] PEG 8000, 100 mM HEPES pH 7.6) and equilibrated by vapor diffusion against 400 μL of well solution. The harvested crystals were soaked in cryoprotectant solution (well solution supplemented with 20% [*v/v*] glycerol) before flash cooling in liquid nitrogen. The oscillation data collection was performed at the National Synchrotron Light Source II beamline 17-ID-1 (AMX) equipped with an Eiger 9M detector at 100 K, an oscillation range of 0.1° per frame, a total of wedge of 180°, and a wavelength of 0.920126 Å.

The diffraction images were reduced using XDS (Kabsch, 2010). The R_{free} set was generated from 5% of the reflections in thin resolution shells using Phenix reflection file editor. In the case of Cfl2 and wild-type Cfl1, initial phases were obtained by molecular replacement with a Cif monomer (PDB ID 3KD2, chain A) as a search model using Phaser. In the case of Cfl1-D123S, a monomer of wild-type Cfl1 structure was used as the search model. Iterative automatic (with torsion-angle NCS restraints) and manual model refinement was performed using phenix.refine and Coot (Liebschner et al., 2019; Emsley et al., 2010).

4.8. Rosetta analysis

All calculations were performed using RosettaScripts (Fleishman et al., 2011) with Rosetta build version 2020.20.post.dev+53.master.64d08bbfc5f. Briefly, protein models determined by X-ray crystallography were prepared using the Fast Relax (Khatib et al., 2011) algorithm with the Rosetta-ICO (a.k.a. beta_nov16) energy function (Pavlovicz et al., 2020) using heavy atom coordinate constraints (see supplementary material for the pre-relax xml protocol); ten decoys were generated and the best scoring model was used for interface analysis. For each protein-protein interface, the shape complementarity (Lawrence and Colman, 1993), change in solvent-accessible surface area (total, polar, and nonpolar area), and binding energy (ΔΔG) were calculated (see supplementary material for the interface analysis xml protocol).

We approximated residue burial using the sidechain neighbor counts method (Bhardwaj et al., 2016). Briefly, a cone is placed on the c_α-c_β vector for each residue under consideration, and any residue within the defined cone is counted as a neighbor. This metric was calculated through the RosettaScripts interface using the Sidechain Neighbor Count Metric, which was created for this work.

4.9. Normal Mode Analysis

The Bio3D package as implemented in R was used to carry out NMA using the c-alpha force-field and the nma() command (Grant et al., 2006; Skjaerven et al., 2014; R Core Team, 2018). The deformation energies displayed in Fig. 9 were calculated using the command deformations.nma() (Hinsen, 1998) and summed over the first three modes for each protein. In the case of the "*ex circulum*" Cfl1 and Cfl2 dimers, the analysis was performed on the dimer subunit that was extracted from its respective oligomer.

4.10. Evolutionary conservation analysis

The conservation analysis was performed by the ConSurf online server using the UniRef90 database (Ashkenazy et al., 2016; Landau et al., 2005). The multiple sequence alignment used for calculating conservation scores was automatically generated by ConSurf and had to include at least 100 "homologous" sequences to ensure reliability. In the case of aCif, the minimum threshold for percent sequence identity was lowered from 35% to 30% in order to obtain more than 100 "homologous" sequences. The normalized residue conservation scores were binned by ConSurf and colored according to a 9-shade purple-white-green scale.

4.11. Accession numbers

The coordinates and structure factors for wild-type Cfl1, Cfl1-D123S, and Cfl2 structures are available in the Protein Data Bank under PDB ID: 7JQX, 7JQY, and 7JQZ, respectively.

CRediT authorship contribution statement

Noor M. Taher: Conceptualization, Investigation, Formal analysis, Visualization, Data curation, Writing – original draft, Project administration, Writing – review & editing. **Kelli L. Hvorecny:** Investigation, Writing – review & editing. **Cassandra M. Burke:** Investigation, Writing – review & editing. **Morgan S.A. Gilman:** Investigation, Writing – review & editing. **Gary E. Heussler:** Investigation, Writing – review & editing. **Jared Adolf-Bryfogle:** Methodology, Software, Data curation, Writing – review & editing. **Christopher D. Bahl:** Conceptualization, Methodology, Data curation, Resources, Writing – review & editing. **George A. O'Toole:** Conceptualization, Resources, Funding acquisition, Writing – review & editing. **Dean R. Madden:** Conceptualization, Writing – original draft, Supervision, Project administration, Funding acquisition, Writing – review & editing, All Authors: Writing - Review & Editing.

Declaration of competing interest

The authors declare that they have no known competing financial interests or personal relationships that could have appeared to influence the work reported in this paper.

Acknowledgements

We would like to thank Dr. Sherry Kuchma for helpful advice on RT-qPCR experiments, and Kelsie Leary for training with CD spectroscopy. We thank Drs. Louisa Howard, Maxime Guinel, Charles Midgett, and Charles Daghlian for electron microscopy training, advice, and assistance. We would also like to thank Drs. Vivian Stojanoff and Jean Jakoncic at the AMX and SSRL beamlines for advice and support with collection of crystal diffraction data. We are grateful to the members of the Madden lab for helpful discussions and suggestions.

This work was supported by the National Institutes of Health grants R01-AI091699, R01-GM113240, R37-AI83256, P20-GM113132, P30-DK117469, P30-GM133893, US Department of Energy contracts DE-SC0012704 and KP1605010, and the Cystic Fibrosis Foundation grant STANTO19R0.

Appendix A. Supplementary data

Supplementary data to this article can be found online at https://doi.org/10.1016/j.crstbi.2021.02.002.

References

Agodi, A., Barchitta, M., Giannino, V., Collura, A., Pensabene, T., Garlaschi, M.L., Pasquarella, C., Luzzaro, F., Sinatra, F., Mahenthiralingam, E., Stefani, S., 2002. *Burkholderia cepacia* complex in cystic fibrosis and non-cystic fibrosis patients: identification of a cluster of epidemic lineages. J. Hosp. Infect. 50, 188–195.

Ashkenazy, H., Abadi, S., Martz, E., Chay, O., Mayrose, I., Pupko, T., Ben-Tal, N., 2016. ConSurf 2016: an improved methodology to estimate and visualize evolutionary conservation in macromolecules. Nucleic Acids Res. 44, W344–W350.

Bahl, C.D., Madden, D.R., 2012. *Pseudomonas aeruginosa* Cif defines a distinct class of a/b epoxide hydrolases utilizing a His/Tyr ring-opening pair. Protein Pept. Lett. 19, 186–193.

Bahl, C.D., Morisseau, C., Bomberger, J.M., Stanton, B.A., Hammock, B.D., O'Toole, G.A., Madden, D.R., 2010. Crystal structure of the cystic fibrosis transmembrane conductance regulator inhibitory factor Cif reveals novel active-site features of an epoxide hydrolase virulence factor. J. Bacteriol. 192, 1785–1795.

Bahl, C.D., Hvorecny, K.L., Bridges, A.A., Ballok, A.E., Bomberger, J.M., Cady, K.C., O'Toole, G.A., Madden, D.R., 2014. Signature motifs identify an *Acinetobacter* Cif virulence factor with epoxide hydrolase activity. J. Biol. Chem. 289, 7460–7469.

Ballok, A.E., Bahl, C.D., Dolben, E.L., Lindsay, A.K., St Laurent, J.D., Hogan, D.A., Madden, D.R., O'Toole, G.A., 2012. Epoxide-mediated CifR repression of cif gene expression utilizes two binding sites in *Pseudomonas aeruginosa*. J. Bacteriol. 194, 5315–5324.

Barnych, B., Singh, N., Negrel, S., Zhang, Y., Magis, D., Roux, C., Hua, X., Ding, Z., Morisseau, C., Tantillo, D.J., Siegel, J.B., Hammock, B.D., 2020. Development of potent inhibitors of the human microsomal epoxide hydrolase. Eur. J. Med. Chem. 193, 112206.

Belchis, D.A., Simpson, E., Colby, T., 2000. Histopathologic features of *Burkholderia cepacia* pneumonia in patients without cystic fibrosis. Mod. Pathol. 13, 369–372.

Bendigiri, C., Zinjarde, S., RaviKumar, A., 2017. Ylehd, an epoxide hydrolase with promiscuous haloalkane dehalogenase activity from tropical marine yeast *Yarrowia lipolytica* is induced upon xenobiotic stress. Sci. Rep. 7, 11887.

Bergendahl, L.T., Marsh, J.A., 2017. Functional determinants of protein assembly into homomeric complexes. Sci. Rep. 7, 4932.

Bertani, G., 1951. Studies on lysogenesis. I. The mode of phage liberation by lysogenic *Escherichia coli*. J. Bacteriol. 62, 293–300.

Bhardwaj, G., Mulligan, V.K., Bahl, C.D., Gilmore, J.M., Harvey, P.J., Cheneval, O., Buchko, G.W., Pulavarti, S.V., Kaas, Q., Eletsky, A., Huang, P.S., Johnsen, W.A., Greisen, P.J., Rocklin, G.J., Song, Y., Linsky, T.W., Watkins, A., Rettie, S.A., Xu, X., Carter, L.P., Bonneau, R., Olson, J.M., Coutsias, E., Correnti, C.E., Szyperski, T., Craik, D.J., Baker, D., 2016. Accurate *de novo* design of hyperstable constrained peptides. Nature 538, 329–335.

Boehr, D.D., D'Amico, R.N., O'Rourke, K.F., 2018. Engineered control of enzyme structural dynamics and function. Protein Sci. 27, 825–838.

Cedrone, F., Bhatnagar, T., Baratti, J.C., 2005. Colorimetric assays for quantitative analysis and screening of epoxide hydrolase activity. Biotechnol. Lett. 27, 1921–1927.

Chen, J.H., Xiang, W., Cao, K.X., Lu, X., Yao, S.C., Hung, D., Huang, R.S., Li, L.B., 2020. Characterization of volatile organic compounds emitted from endophytic

Burkholderia cenocepacia ETR-B22 by SPME-GC-MS and their inhibitory activity against various plant fungal pathogens. Molecules 25, Article 3765.
Decker, M., Arand, M., Cronin, A., 2009. Mammalian epoxide hydrolases in xenobiotic metabolism and signalling. Arch. Toxicol. 83, 297–318.
Emsley, P., Lohkamp, B., Scott, W.G., Cowtan, K., 2010. Features and development of Coot. Acta Crystallogr. D Biol. Crystallogr. 66, 486–501.
Fillgrove, K.L., Pakhomova, S., Newcomer, M.E., Armstrong, R.N., 2003. Mechanistic diversity of fosfomycin resistance in pathogenic microorganisms. J. Am. Chem. Soc. 125, 15730–15731.
Fleishman, S.J., Leaver-Fay, A., Corn, J.E., Strauch, E.M., Khare, S.D., Koga, N., Ashworth, J., Murphy, P., Richter, F., Lemmon, G., Meiler, J., Baker, D., 2011. RosettaScripts: a scripting language interface to the Rosetta macromolecular modeling suite. PLoS One 6, e20161.
Flitter, B.A., Hvorecny, K.L., Ono, E., Eddens, T., Yang, J., Kwak, D.H., Bahl, C.D., Hampton, T.H., Morisseau, C., Hammock, B.D., Liu, X., Lee, J.S., Kolls, J.K., Levy, B.D., Madden, D.R., Bomberger, J.M., 2017. *Pseudomonas aeruginosa* sabotages the generation of host proresolving lipid mediators. Proc. Natl. Acad. Sci. U. S. A. 114, 136–141.
Grant, B.J., Rodrigues, A.P., ElSawy, K.M., McCammon, J.A., Caves, L.S., 2006. Bio3d: an R package for the comparative analysis of protein structures. Bioinformatics 22, 2695–2696.
Hinsen, K., 1998. Analysis of domain motions by approximate normal mode calculations. Proteins 33, 417–429.
Hinsley, A.P., Stanley, N.R., Palmer, T., Berks, B.C., 2001. A naturally occurring bacterial Tat signal peptide lacking one of the 'invariant' arginine residues of the consensus targeting motif. FEBS Lett. 497, 45–49.
Huang, Y., Wong, P.T.W., 1998. Effect of *Burkholderia* (*Pseudomonas*) *cepacia* and soil type on the control of crown rot in wheat. Plant Soil 203, 103–108.
Hvorecny, K.L., Bahl, C.D., Kitamura, S., Lee, K.S.S., Hammock, B.D., Morisseau, C., Madden, D.R., 2017. Active-site flexibility and substrate specificity in a bacterial virulence factor: crystallographic snapshots of an epoxide hydrolase. Structure 25, 697–707.
Hvorecny, K.L., Dolben, E., Moreau-Marquis, S., Hampton, T.H., Shabaneh, T.B., Flitter, B.A., Bahl, C.D., Bomberger, J.M., Levy, B.D., Stanton, B.A., Hogan, D.A., Madden, D.R., 2018. An epoxide hydrolase secreted by *Pseudomonas aeruginosa* decreases mucociliary transport and hinders bacterial clearance from the lung. Am. J. Physiol. Lung Cell Mol. Physiol. 314, L150–L156.
Ignatova, Z., Hornle, C., Nurk, A., Kasche, V., 2002. Unusual signal peptide directs penicillin amidase from *Escherichia coli* to the Tat translocation machinery. Biochem. Biophys. Res. Commun. 291, 146–149.
Jacobs, M.H., Van den Wijngaard, A.J., Pentenga, M., Janssen, D.B., 1991. Characterization of the epoxide hydrolase from an epichlorohydrin-degrading *Pseudomonas sp*. Eur. J. Biochem. 202, 1217–1222.
Jacobs, J.L., Fasi, A.C., Ramette, A., Smith, J.J., Hammerschmidt, R., Sundin, G.W., 2008. Identification and onion pathogenicity of *Burkholderia cepacia* complex isolates from the onion rhizosphere and onion field soil. Appl. Environ. Microbiol. 74, 3121–3129.
Juhasz, A.L., Britz, M.L., Stanley, G.A., 1997. Degradation of fluoranthene, pyrene, benz[*α*]anthracene and dibenz[*a,h*]anthracene by *Burkholderia cepacia*. J. Appl. Microbiol. 83, 189–198.
Jung, F., Schulz, C., Blaschke, F., Muller, D.N., Mrowietz, C., Franke, R.P., Lendlein, A., Schunck, W.H., 2012. Effect of cytochrome P450-dependent epoxyeicosanoids on Ristocetin-induced thrombocyte aggregation. Clin. Hemorheol. Microcirc. 52, 403–416.
Kabsch, W., 2010. XDS. Acta Crystallogr. D Biol. Crystallogr. 66, 125–132.
Kalferstova, L., Kolar, M., Fila, L., Vavrova, J., Drevinek, P., 2015. Gene expression profiling of *Burkholderia cenocepacia* at the time of cepacia syndrome: loss of motility as a marker of poor prognosis? J. Clin. Microbiol. 53, 1515–1522.
Kamp, F., Hamilton, J.A., 2006. How fatty acids of different chain length enter and leave cells by free diffusion. Prostaglandins Leukot. Essent. Fatty Acids 75, 149–159.
Khatib, F., Cooper, S., Tyka, M.D., Xu, K., Makedon, I., Popovic, Z., Baker, D., Players, F., 2011. Algorithm discovery by protein folding game players. Proc. Natl. Acad. Sci. U. S. A. 108, 18949–18953.
Khodai-Kalaki, M., Andrade, A., Fathy Mohamed, Y., Valvano, M.A., 2015. *Burkholderia cenocepacia* lipopolysaccharide modification and flagellin glycosylation affect virulence but not innate immune recognition in plants. mBio 6, e00679.
Kim, T.H., Mehrabi, P., Ren, Z., Sljoka, A., Ing, C., Bezginov, A., Ye, L., Pomes, R., Prosser, R.S., Pai, E.F., 2017. The role of dimer asymmetry and protomer dynamics in enzyme catalysis. Science 355. Article eaag2355.
Krumme, M.L., Timmis, K.N., Dwyer, D.F., 1993. Degradation of trichloroethylene by *Pseudomonas cepacia* G4 and the constitutive mutant strain G4 5223 PR1 in aquifer microcosms. Appl. Environ. Microbiol. 59, 2746–2749.
Landau, M., Mayrose, I., Rosenberg, Y., Glaser, F., Martz, E., Pupko, T., Ben-Tal, N., 2005. ConSurf 2005: the projection of evolutionary conservation scores of residues on protein structures. Nucleic Acids Res. 33, W299–W302.
Lau, Y.K., Baytshtok, V., Howard, T.A., Fiala, B.M., Johnson, J.M., Carter, L.P., Baker, D., Lima, C.D., Bahl, C.D., 2018. Discovery and engineering of enhanced SUMO protease enzymes. J. Biol. Chem. 293, 13224–13233.
Laue, T., Shah, B., Ridgeway, T., Pelletier, S., 1992. Computer-aided interpretation of sedimentation data for proteins. In: Harding, S.E., Rowe, A.J., Horton, J.C. (Eds.), Analytical Ultracentrifugation in Biochemistry and Polymer Science. Royal Society of Chemistry, Cambridge, pp. 90–125.
Lawrence, M.C., Colman, P.M., 1993. Shape complementarity at protein/protein interfaces. J. Mol. Biol. 234, 946–950.
Liebschner, D., Afonine, P.V., Baker, M.L., Bunkoczi, G., Chen, V.B., Croll, T.I., Hintze, B., Hung, L.W., Jain, S., McCoy, A.J., Moriarty, N.W., Oeffner, R.D., Poon, B.K., Prisant, M.G., Read, R.J., Richardson, J.S., Richardson, D.C., Sammito, M.D., Sobolev, O.V., Stockwell, D.H., Terwilliger, T.C., Urzhumtsev, A.G., Videau, L.L., Williams, C.J., Adams, P.D., 2019. Macromolecular structure determination using X-rays, neutrons and electrons: recent developments in Phenix. Acta Crystallogr. D Struct. Biol. 75, 861–877.
Light, S.H., Cahoon, L.A., Mahasenan, K.V., Lee, M., Boggess, B., Halavaty, A.S., Mobashery, S., Freitag, N.E., Anderson, W.F., 2017. Transferase versus hydrolase: the role of conformational flexibility in reaction specificity. Structure 25, 295–304.
MacEachran, D.P., Ye, S., Bomberger, J.M., Hogan, D.A., Swiatecka-Urban, A., Stanton, B.A., O'Toole, G.A., 2007. The *Pseudomonas aeruginosa* secreted protein PA2934 decreases apical membrane expression of the cystic fibrosis transmembrane conductance regulator. Infect. Immun. 75, 3902–3912.
MacEachran, D.P., Stanton, B.A., O'Toole, G.A., 2008. Cif is negatively regulated by the TetR family repressor CifR. Infect. Immun. 76, 3197–3206.
Madacki, J., Laval, F., Grzegorzewicz, A., Lemassu, A., Zahorszka, M., Arand, M., McNeil, M., Daffe, M., Jackson, M., Laneelle, M.A., Kordulakova, J., 2018. Impact of the epoxide hydrolase EphD on the metabolism of mycolic acids in mycobacteria. J. Biol. Chem. 293, 5172–5184.
Mehrabi, P., Di Pietrantonio, C., Kim, T.H., Sljoka, A., Taverner, K., Ing, C., Kruglyak, N., Pomes, R., Pai, E.F., Prosser, R.S., 2019a. Substrate-based allosteric regulation of a homodimeric enzyme. J. Am. Chem. Soc. 141, 11540–11556.
Mehrabi, P., Schulz, E.C., Dsouza, R., Muller-Werkmeister, H.M., Tellkamp, F., Miller, R.J.D., Pai, E.F., 2019b. Time-resolved crystallography reveals allosteric communication aligned with molecular breathing. Science 365, 1167–1170.
Needleman, S.B., Wunsch, C.D., 1970. A general method applicable to the search for similarities in the amino acid sequence of two proteins. J. Mol. Biol. 48, 443–453.
Pavlovicz, R., Park, H., DiMaio, F., 2020. Efficient consideration of coordinated water molecules improves computational protein-protein and protein-ligand docking discrimination. PLoS Comput. Biol. 16, e1008103.
Pintar, S., Borisek, J., Usenik, A., Perdih, A., Turk, D., 2020. Domain sliding of two *Staphylococcus aureus* N-acetylglucosaminidases enables their substrate-binding prior to its catalysis. Commun. Biol. 3, 178.
Rodrigue, A., Chanal, A., Beck, K., Muller, M., Wu, L.F., 1999. Co-translocation of a periplasmic enzyme complex by a hitchhiker mechanism through the bacterial tat pathway. J. Biol. Chem. 274, 13223–13228.
Schomaker, V., Trueblood, K., 1968. On the rigid-body motion of molecules in crystals. Acta Crystallogr. B Struct. Crystallogr. Cryst. Chem. 24, 63–76.
Schuck, P., 2000. Size-distribution analysis of macromolecules by sedimentation velocity ultracentrifugation and Lamm equation modeling. Biophys. J. 78, 1606–1619.
Scoffone, V.C., Chiarelli, L.R., Trespidi, G., Mentasti, M., Riccardi, G., Buroni, S., 2017. *Burkholderia cenocepacia* infections in cystic fibrosis patients: drug resistance and therapeutic approaches. Front. Microbiol. 8, 1592.
Scortti, M., Han, L., Alvarez, S., Leclercq, A., Moura, A., Lecuit, M., Vazquez-Boland, J., 2018. Epistatic control of intrinsic resistance by virulence genes in *Listeria*. PLoS Genet. 14, e1007525.
Skjaerven, L., Yao, X.Q., Scarabelli, G., Grant, B.J., 2014. Integrating protein structural dynamics and evolutionary analysis with Bio3D. BMC Bioinf. 15, 399.
Strong, M., Sawaya, M.R., Wang, S., Phillips, M., Cascio, D., Eisenberg, D., 2006. Toward the structural genomics of complexes: crystal structure of a PE/PPE protein complex from *Mycobacterium tuberculosis*. Proc. Natl. Acad. Sci. U. S. A. 103, 8060–8065.
Tang, G., Peng, L., Baldwin, P.R., Mann, D.S., Jiang, W., Rees, I., Ludtke, S.J., 2007. EMAN2: an extensible image processing suite for electron microscopy. J. Struct. Biol. 157, 38–46.
Tartoff, K., Hobbs, C., 1987. Improved Media for Growing Plasmid and Cosmid Clones, 9. Bethesda Research Laboratories, p. 12.
R Core Team, 2018. R: a Language and Environment for Statistical Computing. R Foundation for Statistical Computing, Vienna, Austria. Available online at. https://www.R-project.org/.
Vaclavikova, R., Hughes, D.J., Soucek, P., 2015. Microsomal epoxide hydrolase 1 (EPHX1): gene, structure, function, and role in human disease. Gene 571, 1–8.
van Loo, B., Kingma, J., Arand, M., Wubbolts, M.G., Janssen, D.B., 2006. Diversity and biocatalytic potential of epoxide hydrolases identified by genome analysis. Appl. Environ. Microbiol. 72, 2905–2917.
VanRollins, M., 1995. Epoxygenase metabolites of docosahexaenoic and eicosapentaenoic acids inhibit platelet aggregation at concentrations below those affecting thromboxane synthesis. J. Pharmacol. Exp. Therapeut. 274, 798–804.
Vivoli, M., Pang, J., Harmer, N.J., 2017. A half-site multimeric enzyme achieves its cooperativity without conformational changes. Sci. Rep. 7, 16529.
Wagner, K.M., McReynolds, C.B., Schmidt, W.K., Hammock, B.D., 2017. Soluble epoxide hydrolase as a therapeutic target for pain, inflammatory and neurodegenerative diseases. Pharmacol. Ther. 180, 62–76.
Yamada, T., Morisseau, C., Maxwell, J.E., Argiriadi, M.A., Christianson, D.W., Hammock, B.D., 2000. Biochemical evidence for the involvement of tyrosine in epoxide activation during the catalytic cycle of epoxide hydrolase. J. Biol. Chem. 275, 23082–23088.
Ye, D., Zhang, D., Oltman, C., Dellsperger, K., Lee, H.C., VanRollins, M., 2002. Cytochrome p-450 epoxygenase metabolites of docosahexaenoate potently dilate coronary arterioles by activating large-conductance calcium-activated potassium channels. J. Pharmacol. Exp. Therapeut. 303, 768–776.
Zhang, Y., Oltman, C.L., Lu, T., Lee, H.C., Dellsperger, K.C., VanRollins, M., 2001. EET homologs potently dilate coronary microvessels and activate BK(Ca) channels. Am. J. Physiol. Heart Circ. Physiol. 280, H2430–H2440.
Zou, J., Hallberg, B.M., Bergfors, T., Oesch, F., Arand, M., Mowbray, S.L., Jones, T.A., 2000. Structure of *Aspergillus niger* epoxide hydrolase at 1.8 Å resolution: implications for the structure and function of the mammalian microsomal class of epoxide hydrolases. Structure 8, 111–122.